

ADVANCED MATERIALS

Supporting Information

for *Adv. Mater.*, DOI: 10.1002/adma.201202932

Plasmid-Templated Shape Control of Condensed DNA–Block
Copolymer Nanoparticles

*Xuan Jiang, Wei Qu, Deng Pan, Yong Ren, John-Michael
Williford, Honggang Cui, Erik Luijten,* and Hai-Quan Mao**

SUPPORTING INFORMATION

**Plasmid-Templated Shape Control of Condensed DNA–Block
Copolymer Nanoparticles**

Xuan Jiang^{a,b,#}, Wei Qu^{c,#}, Deng Pan^d, Yong Ren^{a,b}, John-Michael Williford^d, Honggang Cui^e,
Erik Luijten^{c,f,1}, Hai-Quan Mao^{a,b,1}

^aDepartment of Materials Science and Engineering, Whiting School of Engineering, Johns Hopkins University, Baltimore, Maryland 21218, USA;

^bTranslational Tissue Engineering Center and Whitaker Biomedical Engineering Institute, Johns Hopkins School of Medicine, Baltimore, Maryland 21287, USA;

^cDepartment of Materials Science and Engineering, Northwestern University, Evanston, Illinois 60208, USA;

^dDepartment of Biomedical Engineering, Johns Hopkins School of Medicine, Baltimore, Maryland 21205, USA;

^eDepartment of Chemical and Biomolecular Engineering, Whiting School of Engineering, Johns Hopkins University, Baltimore, Maryland 21218, USA;

^fDepartment of Engineering Sciences and Applied Mathematics, Northwestern University, Evanston, Illinois 60208, USA.

[#]These authors contributed equally to this work.

¹To whom correspondence should be addressed.

Email: luijten@northwestern.edu and hmao@jhu.edu

1. Self-assembly of PEG-*b*-PPA/DNA Micellar Nanoparticles

1.1. Synthesis of PEG_{10K}-*b*-PPA_{4K} block copolymer and PPA-DPA

PEG_{10K}-*b*-PPA_{4K} polymer was synthesized through ring-opening coordination polymerization (**Fig. S1**). Methoxy-polyethylene (mPEG, MW 9.5 kDa, 1.9 g, 0.2 mmol) was first dried by azeotropic distillation in toluene to remove water associated with the PEG chains and then incubated with equal amount of triisobutylaluminum in 20 ml of dichloromethane for 1 h. The polymerization of 4-alkyl-2-oxo-2-hydro-1,3,2-dioxaphospholane was initiated by injecting 5.3 g (43 mmol) of monomer into initiator solution pre-cooled in an ice bath. The mixture was stirred at 0°C for 48 h. *Precursor Polymer 1* was obtained by removing solvent under vacuum at room temperature and subsequently dissolved in 40 ml of anhydrous DMF under argon. To this solution was added 37.8 g (86 mmol) of N¹,N⁹-bis(trifluoroacetyl)dipropyltriamine (TFA-DPA) [S1], followed by addition of 48.0 ml (340 mmol) of anhydrous triethylamine and 33.3 ml (340 mmol) of anhydrous CCl₄. The mixture was stirred at 0°C for 30 min, then at room temperature for 24 h. The reaction mixture was

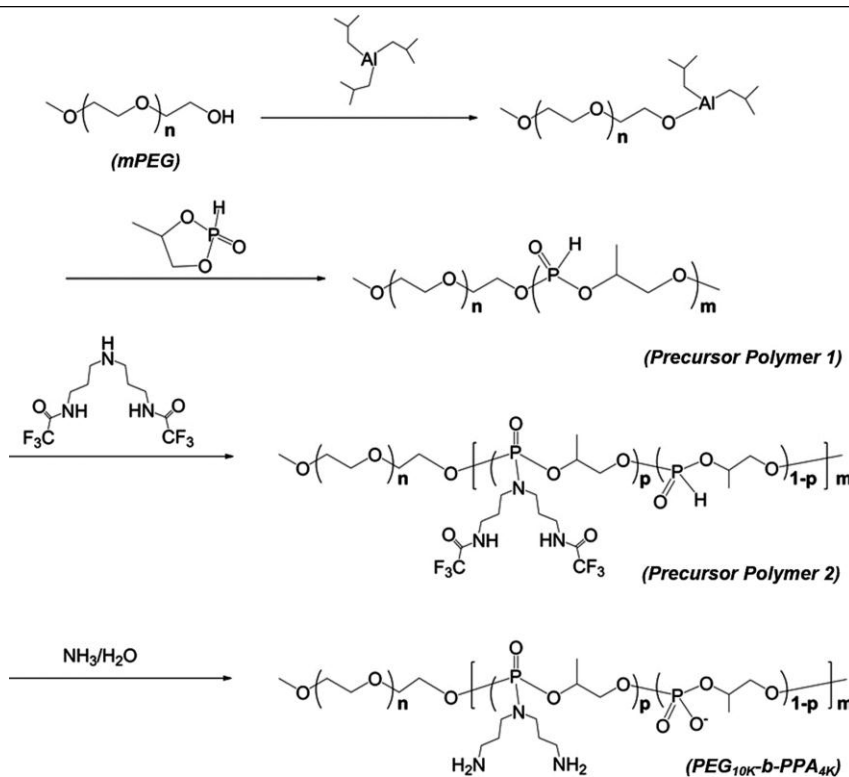


Figure S1. Synthesis scheme of PEG-*b*-PPA. The number average molecular weights of PEG and PPA blocks were 9.5 kDa and 4.15 kDa, respectively. The grafting density p can be controlled in a range of 50% to 70%.

precipitated into ether and dried under vacuum to yield *Precursor Polymer 2*, which was then resuspended in 25% ammonia solution and stirred at 60°C for 16 h. The solution was concentrated and dialyzed in dialysis tubing (MWCO 3500, Spectrapor, Spectrum Labs, CA) against distilled water for 2 days. The unreacted mPEG was removed by ion-exchange column (Sephadex C25, Sigma) using DI water as an eluent. Sodium hydroxide (0.1 mol/l) was used to elute the PEG-*b*-PPA polymer. The PEG-*b*-PPA was obtained after neutralization, dialysis, and lyophilization (yield 30–40%).

PPA-DPA polymer was synthesized according to our previous report [S2]. The molecular weights of PEG-*b*-PPA and PPA-DPA polymers were determined using an Agilent 1200 Series Isocratic LC System coupled with a multi-angle light scattering detector (MiniDawn, Wyatt Technology, Santa Barbara, CA). A dn/dc value of 1.4 was used for all PEG-*b*-PPA samples. Sodium acetate buffer (HAc-NaAc 0.5 M, pH 4.8) was used as the mobile phase (flow rate 0.5 ml/min). The $^1\text{H-NMR}$ spectra were recorded on a Bruker 400 MHz NMR (Bruker, Billerica, MA). The grafting degree of DPA for PEG-*b*-PPA and PPA-DPA polymers was obtained by comparing the integral of peaks at δ 1.1–1.4 ppm (CH_3 - in the backbone) and δ 1.9–2.0 ppm ($-\text{CH}_2\text{CH}_2\text{CH}_2-$ in the grafted side chains). The structural characteristics of PEG-*b*-PPA and PPA-DPA (hereafter referred to as PPA) polymers are listed in **Table S1**.

Table S1. Structural characteristics of PEG_{10K}-*b*-PPA_{4K} and PPA-DPA polymers.

Polymer carrier	PEG _{10K} - <i>b</i> -PPA _{4K}	PPA-DPA _{4K} [a]
M_n	13,650	4,400
Polydispersity	1.08	1.64
M_n of PEG block	9,500	N.A.
M_n of PPA block	4,150	4,400
Grafting degree of DPA (%)	54.3	54.7

[a] Hereafter referred to as PPA_{4K}.

1.2. Amplification and purification of plasmid DNA

VR1255C plasmid DNA (6.4 kb) encoding firefly luciferase driven by cytomegalovirus promoter was provided as a gift by Vical (San Diego, CA). The plasmid DNA was amplified in *E. coli* DH5 α and purified with a QIAGEN EndoFree Giga kit (QIAGEN, Valencia, CA).

1.3. Preparation of PEG_{10K}-*b*-PPA_{4K}/DNA micelles in DMF–water mixtures

For a typical preparation, VR1255 plasmid DNA (25 μ g) was first dissolved in 250 μ l DI water or dimethylformamide (DMF)–water mixtures with different DMF to water volumetric ratios ranging from 0:1, 3:7, 5:5 to 7:3 (v/v). PEG_{10K}-*b*-PPA_{4K} polymer (340.6 μ g, corresponding to an N/P ratio of 8) was also dissolved in 250 μ l DI water or DMF–water mixture at the same DMF fraction. This N/P ratio was selected based on our previous report [S3] showing optimal transfection efficiency at this ratio. To obtain PEG_{10K}-*b*-PPA_{4K}/DNA micelles with different morphologies, plasmid DNA solution was added into PEG_{10K}-*b*-PPA_{4K} polymer solution and the mixture was vortexed for 30 s. The mixture was then incubated at room temperature for 24 h before characterization.

1.4. Transmission electron microscopy (TEM)

Samples were prepared by depositing 10 μ l of PEG_{10K}-*b*-PPA_{4K}/DNA micelle solution on a freshly ionized nickel grid covered by a carbon film. After 10 min, excess liquid was blotted away with filter paper. A drop of 2% uranyl acetate solution (\sim 1 μ l) was then deposited on the nickel grid. After drying at room temperature, the samples were examined on a Tecnai FEI-12 electron microscope.

1.5. Cryogenic TEM (Cryo-TEM)

To prepare samples for Cryo-TEM, 5–10 μ l of micelle solution was placed on a holey carbon film supported on a TEM copper grid (SPI Supplies, West Chester, PA). Following the preset procedure of the FEI Vitrobot vitrification system (FEI Company, Hillsboro, OR), the specimen was blotted and plunged into a liquid ethane reservoir cooled by liquid nitrogen. The vitrified samples were transferred to a Gatan 626 cryoholder and cryo-transfer stage cooled by liquid nitrogen. The specimens were then examined on an FEI Tecnai 12 microscope using a

Gatan cryo-holder system. During observation of the vitrified samples, the cryo-holder temperature was maintained at less than -165°C to prevent sublimation of vitreous water. The images were captured digitally by a Gatan low-dose CCD camera. **Fig. S2** shows that the dimensions and morphologies of these micelles obtained by cryo-TEM imaging agreed well with those obtained with regular TEM (**Fig. 1B–E**).

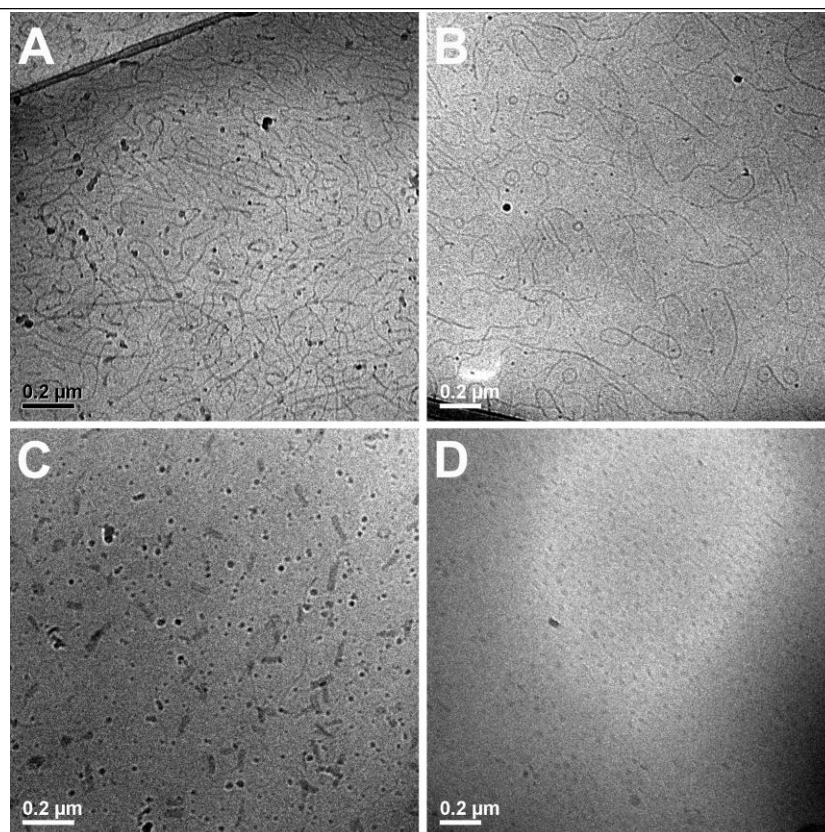


Figure S2. Cryo-TEM images of $\text{PEG}_{10\text{K}}\text{-}b\text{-PPA}_{4\text{K}}/\text{DNA}$ micelles prepared in deionized (DI) water (A) and crosslinked $\text{PEG}_{10\text{K}}\text{-}b\text{-PPA}_{4\text{K}}/\text{DNA}$ micelles (B–D) prepared in DMF–water mixture solvent at an N/P ratio of 8. Crosslinked micelles with different shapes were prepared using thiolated $\text{PEG}_{10\text{K}}\text{-}b\text{-PPA}_{4\text{K}}$ under the same condition as described in Fig. 1 and then crosslinked by aerial oxidation for 48 h, after which DMF was removed from the solution by dialysis against DI water. Cryo-TEM images of the crosslinked micelles initially obtained in DI water (B), 5:5 (v/v) (C), and 7:3 (v/v) (D) DMF–water mixtures. All scale bars represent 200 nm.

1.6. Preparation of PEG_{10K}-*b*-PPA_{4K}/DNA micelles in DMSO–water mixtures

These micelles were prepared according to the same procedure as described in Section 1.3, except that DMF was replaced with DMSO. **Fig. S3** shows the same series of shape changes as those illustrated in **Fig. 1**. Worm-like and ring-like micelles were obtained in water (**Fig. 1B**) and DMSO–water (3:7, v/v) (**Fig. S3A**), short rod-like micelles in DMSO–water (5:5, v/v) (**Fig. S3B**) and spherical micelles in DMSO–water (7:3, v/v) mixtures (**Fig. S3C**).

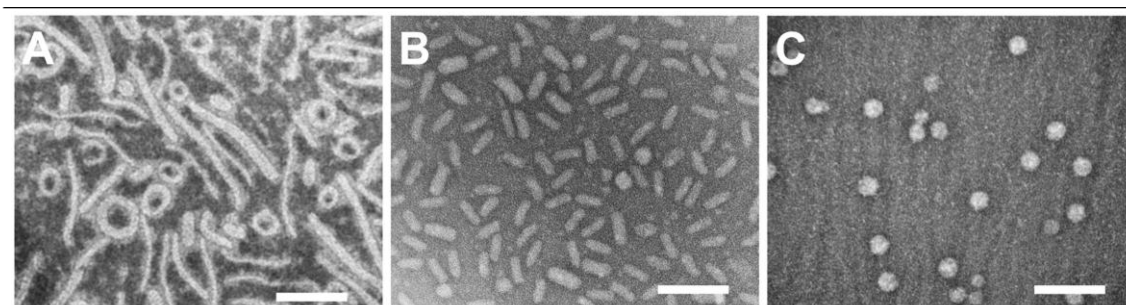


Figure S3. Morphologies of PEG_{10K}-*b*-PPA_{4K}/DNA micelles prepared in 3:7 (v/v) (A), 5:5 (v/v) (B), and 7:3 (v/v) (C) DMSO–water mixture solvent at an N/P ratio (ratio of primary amino groups in PPA block of the copolymer to phosphate groups in DNA) of 8. The micelle solutions were incubated at room temperature for 24 h and then processed for TEM imaging. All scale bars represent 200 nm. These micelles exhibited morphologies similar to those of micelles obtained in DMF–water mixtures at the same mixing ratios.

1.7. Effect of solvent polarity on plasmid DNA morphology

VR1255 plasmid DNA (10 μg) was dissolved in 100 μl DMF–water mixture at different DMF/water volumetric ratios ranging from 1:9 to 7:3. The morphologies of plasmid DNA in DMF–water mixtures with different DMF/water volumetric ratios were then characterized by TEM (**Fig. S4**).

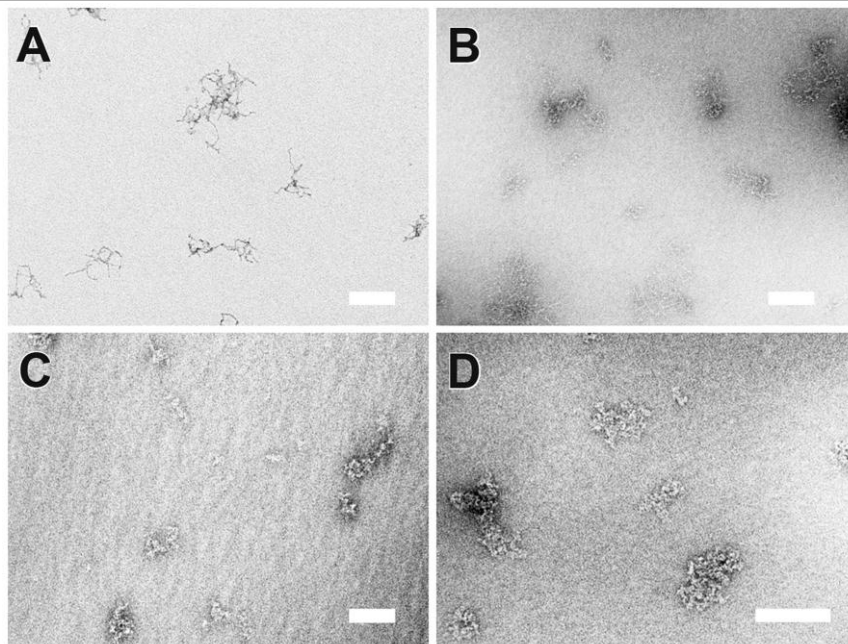


Figure S4. Effect of solvent polarity on the conformation of plasmid DNA in 1:9 (v/v) (A), 3:7 (v/v) (B), 5:5 (v/v) (C), and 7:3 (v/v) (D) DMF–water mixture. The scale bars represent 200 nm. With increasing DMF fraction, plasmid DNA molecules formed more condensed structures with some sizes smaller than 100 nm. However, large aggregates of plasmid DNA molecules with sizes above 200 nm were frequently observed as well.

1.8. Effect of solvent polarity on the shape of PPA_{4K}/DNA nanoparticles

VR1255 plasmid DNA (10 μg) was first dissolved in 100 μl DI water or DMF–water mixture at different DMF/water volumetric ratios. PPA_{4K} polymer (44.6 μg , corresponding to an N/P ratio of 8) was also dissolved in 100 μl DI water or DMF–water mixture at the same DMF fraction. PPA_{4K}/DNA nanoparticles were prepared by adding plasmid DNA solution into PPA_{4K} solution. The mixture was vortexed for 30 s and incubated at room temperature for 2 h. The morphologies of PPA_{4K}/DNA nanoparticles in DMF–water mixtures with different DMF fractions were then characterized by TEM (**Fig. S5**). As seen in the TEM images, spherical and irregularly shaped particles were obtained under all solvent conditions examined, with aggregates observed at higher DMF fraction. No particles with higher aspect ratios were observed, highlighting the importance of PEG segments in controlling the shapes of PEG-*b*-PPA/DNA micelles.

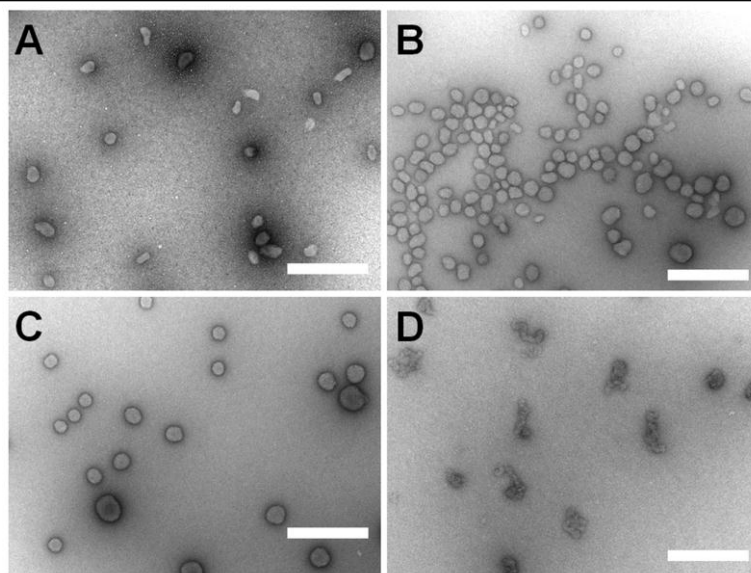


Figure S5. Effect of DMF fraction on the morphology of PPA_{4K}/DNA nanoparticles. PPA_{4K}/DNA nanoparticles were prepared in DI water (A) and 3:7 (v/v) (B), 5:5 (v/v) (C), and 7:3 (v/v) (D) DMF–water mixture. All scale bars represent 200 nm.

2. Computational Methods

2.1 Simulation model

The LAMMPS package was used to perform large-scale molecular dynamics simulations [S4]. In the simulations, the DNA and the PEG-*b*-PPA copolymers were represented by a bead–spring model with a harmonic bond potential,

$$U_{\text{bond}} = 200\varepsilon(r - r_0)^2, \quad (1)$$

where r is the center-to-center distance between two beads connected by a bond and $r_0 = 2^{1/6}\sigma$, with σ the Lennard-Jones (LJ) unit of length and ε the LJ unit of energy. In light of computational efficiency, the plasmid DNA was represented by a bead–spring ring polymer of 80 beads, in which each bead had an electrostatic valency of -1 . To represent the characteristic charge pattern of the PPA block, we simulated the PPA block as 3 beads with charges $(+2, +2, -1)$, *i.e.*, a grafting density of 67%, corresponding to the upper limit of the grafting density in the experiments. The length of the PEG block in the simulation was chosen as 10 beads, all of which were neutral.

Whereas the copolymers were considered fully flexible, an additional harmonic bond-angle potential was applied to the DNA to represent its intrinsic stiffness,

$$U_{\text{angle}} = 4\varepsilon(\theta - \theta_0)^2, \quad (2)$$

where θ is the angle between two adjacent bonds and $\theta_0 = 180^\circ$. With this bond stiffness, the intrinsic persistence length of the DNA is 6.8σ , as determined from the exponential decay length of the bond-angle correlation function of a neutral, linear polymer with the same bond-angle potential [S5]. As a result, the ratio of the intrinsic persistence length to the contour length is approximately three times larger than in the experiments, which we consider acceptable given the simplifications adopted in this semi-quantitative model.

The solvent was simulated implicitly using a Langevin thermostat with damping time 100τ , where τ is the LJ unit of time,

$$\tau = \sqrt{\frac{m\sigma^2}{\varepsilon}}, \quad (3)$$

in which m is the LJ unit of mass. The equations of motion were integrated using the velocity-Verlet algorithm. The temperature was controlled by the Langevin thermostat as well, and set to $T = 1.2\epsilon/k_B$, where k_B is Boltzmann's constant. Following Ref. [S6], the Bjerrum length in water was chosen to be equal to 3σ . As the solvent changes from pure water to DMF–water mixtures at different proportions, the dielectric constant increases (cf. **Table S2**). At the same time, the charge density of the plasmid DNA decreases with increasing DMF fraction [17], as reflected by the ζ potential in **Table S2**.

Table S2. Dielectric constant and ζ potential of plasmid DNA for pure water and for DMF–water mixtures

Solvent Condition	Dielectric Constant [S7]	ζ potential (mV) [17]
Water	79.5	–64
DMF–water (30:70, v/v)	75.0	–58
DMF–water (50:50, v/v)	67.9	–58
DMF–water (70:30, v/v)	57.0	–53

Although the DNA conformation and the mixed nature of the solvent complicate a precise calculation of the surface charge from the ζ potential, it is reasonable to employ the approximation (although strictly valid only for low ζ potential) that surface charge and ζ potential are linearly proportional [S8]. Then, if we also assume that the surface charges on DNA and PPA respond similarly to solvent variation, the variation in surface charge counteracts the variation in dielectric constant and the electrostatic interaction between DNA and PPA blocks varies by only ~5% over the range of DMF/water volumetric ratios tested (with an outlier of 13% for a 3:7 (v/v) DMF–water mixture). Thus, for simplicity we assumed a constant Bjerrum length and constant charge density in our model.

As the DMF concentration increases, the solvent quality for DNA and PPA systematically decreases. Since we employed an implicit solvent, the change from a good to a poor solvent was represented by an increase in the effective attraction between DNA repeat units and between PPA repeat units. Since the PPA blocks and DNA already experience a strong electrostatic interaction, no additional solvent-induced effective attraction between DNA and PPA was imposed. When selecting the relative magnitude of the DNA–DNA attraction and the PPA–PPA

Table S3. Effective attraction strength a_{LJ} (in units of the LJ energy parameter ε) between DNA units and PPA units for different solvent conditions. With increasing DMF fraction, the solvent quality decreases, represented by an increase in a_{LJ} . Since the simulations take place at a temperature $T = 1.2\varepsilon/k_B$, an attraction strength $a_{LJ} = 1.2\varepsilon$ corresponds to $1k_B T$ and $a_{LJ} = 3.6\varepsilon$ corresponds to $3k_B T$.

Solvent Condition	a_{LJ} / ε (DNA)	a_{LJ} / ε (PPA)
Solvent 1	1.2	Purely repulsive
Solvent 2	2.0	0.4
Solvent 3	2.8	0.8
Solvent 4	3.6	1.2

attraction, it must be taken into account that the number of DNA monomers represented by a single DNA bead in the simulations is approximately three times larger than the number of PPA monomers represented by a PPA bead. Consequently, the number of DNA–solvent contacts (per bead in the simulation) is approximately three times larger than the number of PPA–solvent contacts. To reflect this, we set the attraction between PPA units in the poorest solvent (Solvent 4) to one third of the attraction between DNA units. In the coarse-grained modeling adopted here, it was our aim to elucidate the mechanism of micelle shape variation, rather than to realize a precise mapping between different DMF/water ratios onto attractive pair potentials. Thus, we opted to describe this pair potential via a LJ potential with gradually increasing attractive strength. Since attraction strengths above $3k_B T$ are likely to result in a kinetically arrested situation, we chose the four solvents to linearly interpolate between $1k_B T$ and $3k_B T$ for the DNA repeat units. For PPA repeat units, we thus chose the attraction strength in Solvent 4 to be $1k_B T$, which was then decreased linearly to a potential without attraction (i.e., a purely repulsive shifted-truncated LJ potential) in Solvent 1. Given our choice for the temperature, this yielded the parameters listed in **Table S3**. The pair potential was cut off at 2.5σ and shifted at the cutoff to eliminate a discontinuity in the interaction, except for PPA in Solvent 1, for which a

purely repulsive interaction potential was generated by imposing a cutoff at $2^{1/6}\sigma$ and performing a corresponding shift to eliminate a discontinuity at the cutoff. On the other hand, both water and DMF and their mixtures are good solvents for PEG [S9]. We opted against attempting to include minor PEG solubility variations with DMF/water ratio in our model, but instead represented the uniformly good solvent conditions via a purely repulsive shifted-truncated LJ potential with a cutoff $2^{1/6}\sigma$. All other nonbonded short-range interactions (excluded-volume interactions with PPA and ions) were modeled with the same purely repulsive potential. The electrostatic interactions were taken into account using Ewald summation [12–14].

This approach incorporates fluctuation phenomena and, as has been demonstrated for comparable systems [13, 14], permits a rapid, systematic, and independent variation of the relevant variables, and also fully resolves the arrangement of the different constituents (PEG and PPA blocks, plasmid DNA, and counterions) within a micelle. The total number of copolymers is controlled by the charge ratio (ratio of the total net positive charge on the PPA blocks to the total negative charge on the DNA), which we set to 3, i.e., one DNA chain and 80 block copolymers. This is slightly lower than the experimental charge ratio of 4.6, but we confirmed that our results did not vary significantly for charge ratios in the range of 3 to 6. In addition, 160 negative monovalent counterions were present in the system to maintain charge neutrality, without additional salt. All particles were placed in a cubic, periodically replicated simulation cell with linear size 100σ . The electrostatic energies and forces were computed by the Particle–Particle Particle–Mesh (PPPM) Ewald algorithm, with a relative accuracy of 10^{-4} .

2.2 Radius of gyration tensor and asphericity

To quantitatively characterize the shape of the DNA in the simulation, we employed the asphericity introduced in the main text [S10,15,16], which is computed from the eigenvalues λ_1 , λ_2 , and λ_3 of the DNA radius-of-gyration tensor [S11],

$$Q_{\alpha\beta} = \frac{1}{2N^2} \sum_{i,j=1}^N [r_{i,\alpha} - r_{j,\alpha}] [r_{i,\beta} - r_{j,\beta}], \quad (4)$$

where $N = 80$ is the number of beads representing the DNA, and r_i represents the Cartesian coordinate of the i th bead and $\alpha, \beta = 1, 2, 3$ denote Cartesian components.

2.3 Equilibration of the simulations and the use of parallel tempering

The DNA chain, the copolymers, and the counterions initially were randomly placed in the simulation box. To accelerate the equilibration process, initially a shifted and truncated LJ interaction with cutoff $2^{1/6}\sigma$ was used as the only pairwise interaction between any two particles. After an equilibration period of $3 \times 10^3\tau$ with time step 0.01τ , the proper LJ interactions and all electrostatic interactions were switched on, followed by a second equilibration period of $2.4 \times 10^3\tau$. As shown in **Fig. S6**, the structure of the DNA fluctuates between different states. However, in a single run, the switching occurs relatively infrequently, which makes it difficult to obtain an accurate probability distribution for the asphericity. To accelerate the fluctuation between different states, we employed the parallel tempering method [S12]. In this approach, multiple copies of the same system are simulated in parallel, at different temperatures. At fixed intervals, an exchange between configurations simulated at adjacent temperatures is attempted. This approach exploits the larger degree of fluctuations at higher temperatures to provide a pathway for the simulations at the original temperature to transition between states. With increasing interaction strength (decreasing solvent quality), transitions became progressively more difficult and a larger number of parallel simulations were required. The details for the parallel tempering runs are listed in **Table S4**. The temperatures were distributed logarithmically over the interval indicated. Three parallel tempering runs were performed for each solvent, for a sampling period of at least $7.2 \times 10^5\tau$ per run.

Table S4. Simulation details of parallel tempering for different solvent conditions. The number of partitions represents the number of different temperatures at which the system is simulated simultaneously.

Solvent Condition	Temperature range / (ε/k_B)	Number of partitions	Time step / τ	Exchange interval / step
Solvent 1	1.2 to 1.6	12	0.012	4000
Solvent 2	1.2 to 1.8	52	0.012	4000
Solvent 3	1.2 to 2.4	80	0.010	4800
Solvent 4	1.2 to 2.8	92	0.008	6000

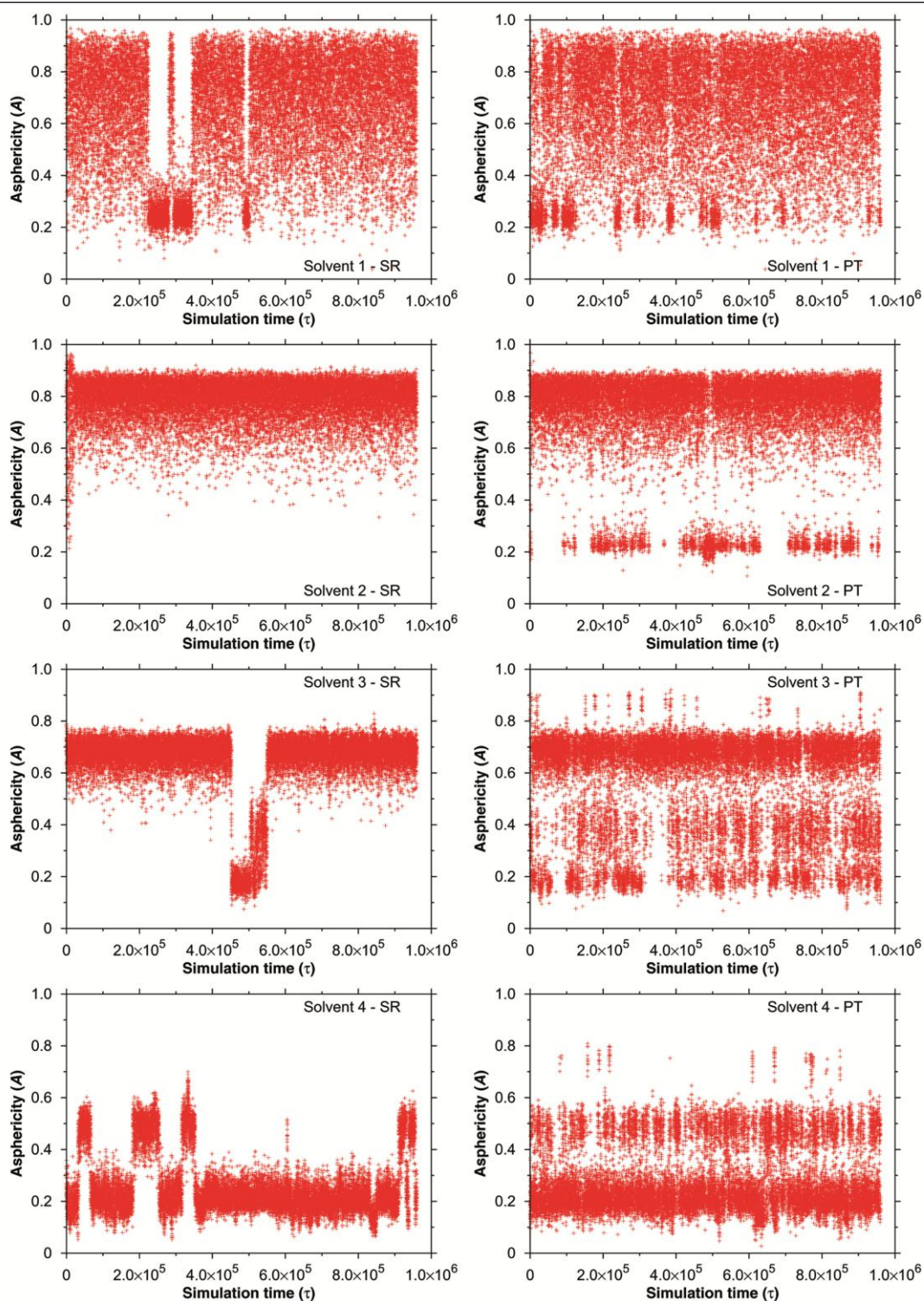


Figure S6. Time evolution of the asphericity of DNA within a PEG-*b*-PPA/DNA micelle in Solvents 1–4 (top to bottom) obtained in a serial run (labeled SR, left-hand column) and via parallel tempering (labeled PT, right-hand column).

2.4 Effect of PEG blocks

Fig. S7 shows the frequency distribution of the asphericity of the plasmid DNA within a PPA/DNA complex (i.e., DNA complexed with a PPA homopolymer) and within a PEG-*b*-PPA/DNA micelle in each of the four different solvents. For DNA condensed with PPA homopolymers, the asphericity peak associated with elongated conformations is absent, demonstrating that without the excluded-volume effect of the PEG blocks, the micelle could not assume an elongated conformation. Furthermore, in Solvents 1–3 the peak corresponding to the toroidal structure is significantly broader for DNA condensed with PPA alone than for DNA condensed with PEG-*b*-PPA copolymers, reflecting stronger structural fluctuations of the PPA/DNA complexes. This reinforces our conclusions regarding the crucial role of the PEG blocks in controlling the shape and uniformity of the micelles.

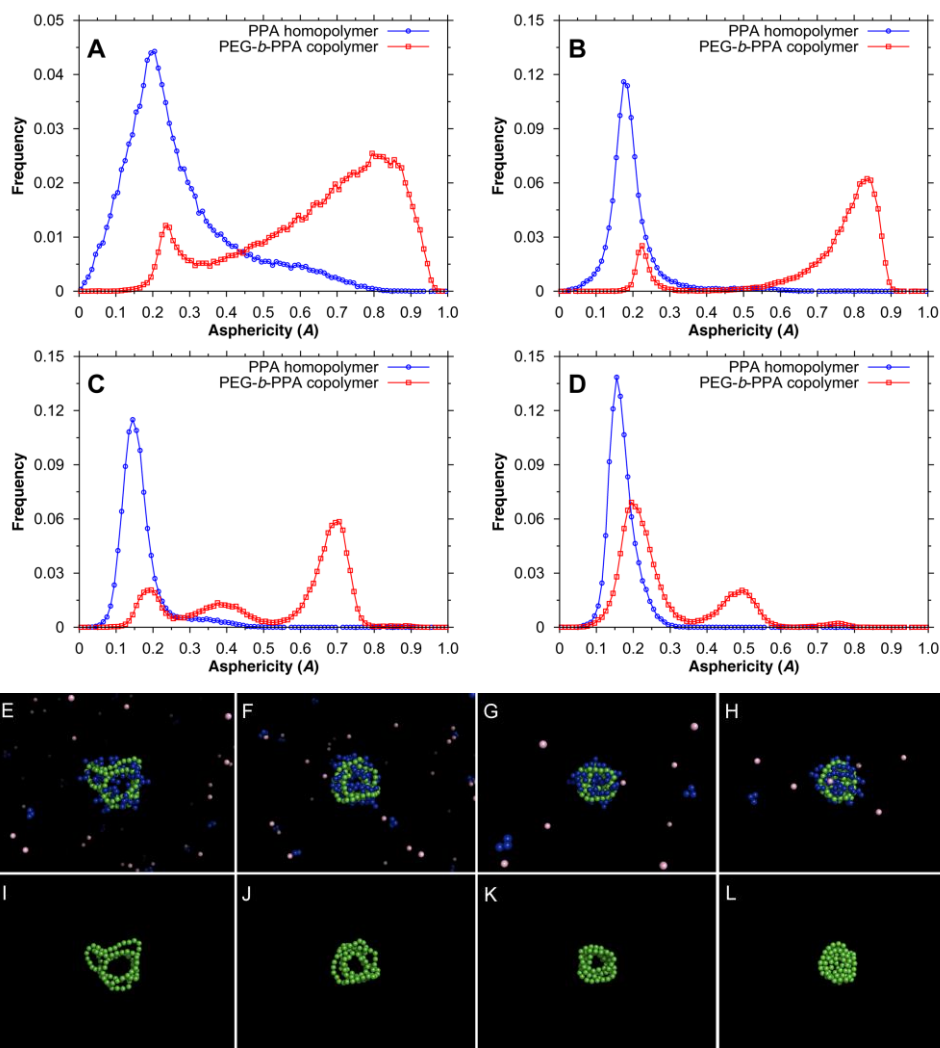


Figure S7. (A–D) Frequency distribution of DNA asphericity in PPA/DNA complexes and in PEG-*b*-PPA/DNA micelles in Solvent 1 (A), Solvent 2 (B), Solvent 3 (C), and Solvent 4 (D). Panels (E–H) show representative images obtained from molecular dynamics simulations of the condensation of plasmid DNA with PPA_{4K} polymer in Solvent conditions 1 through 4, similar to those discussed in Figs. 1 and 2. Panels (I–L) show the same images, in which all PPA segments and counterions have been omitted for clarity.

3. Transformation of Micelle Shape by Titrating Solvent Polarity

PEG_{10K}-*b*-PPA_{4K}/DNA micelles were first prepared in the presence of 7:3 (v/v) DMF–water mixture as described in Section 1.6. DI water was gradually titrated into 500 μl of micelle solution with a syringe pump at a rate of 1 ml/h under stirring. At different DMF fractions, an aliquot of micelle solution was incubated at room temperature for 24 h and processed for TEM imaging (**Fig. 3**). TEM images were analyzed with Image J 1.43. The lengths or diameters of each individual micelle were measured, and the average diameters and standard deviations were calculated from the measurements of 80 to 100 micelles in each sample.

4. Stabilization of Micelle Shapes and Gene Delivery In Vivo

4.1. Preparation of thiolated PEG_{10K}-*b*-PPA_{4K} carrier

PEG_{10K}-*b*-PPA_{4K} polymer (10 mg) was dissolved in 75 mM, pH 8.0 PBS buffer (purged with argon to remove dissolved oxygen) to achieve a concentration of 20 mg/ml. Traut's reagent (0.45 mg) dissolved in DI water at a concentration of 10 mg/ml was mixed with PEG_{10K}-*b*-PPA_{4K} polymer solution and reacted for 2 h at room temperature (**Fig. S8**). The reaction mixture was then dialyzed against 2 mM EDTA solution (purged with argon) for 1 h through a dialysis membrane with MWCO of 3,500 Da. The final product was obtained after lyophilization. The grafting degree of free thiol groups was determined to 18.9% by using 4-(amino-sulfonyl)-7-fluoro-2,1,3-benzoxadiazole (ABD-F) reagent according to a reported method [S13].

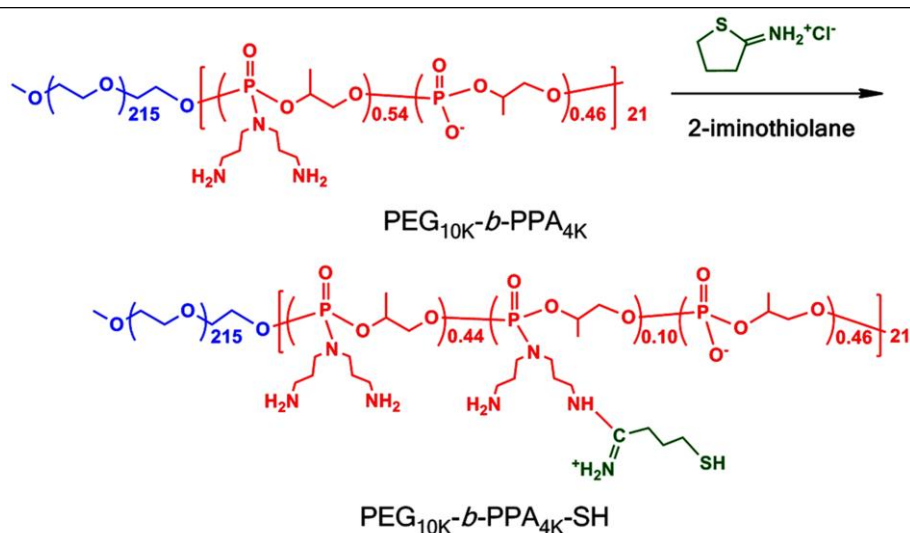


Figure S8. Reaction scheme for preparing thiolated PEG_{10K}-*b*-PPA_{4K} copolymer carrier.

4.2. Preparation of micelles with different shapes with thiolated PEG_{10K}-*b*-PPA_{4K}

To compare the shapes and sizes of uncrosslinked micelles with those shown in Fig. 4, thiolated PEG_{10K}-*b*-PPA_{4K}/DNA micelles were prepared in 7:3 (v/v), 5:5 (v/v), 4:6 (v/v), and 1:9 (v/v) DMF–water mixtures using the same protocol as described in Fig. 4. An aliquot of micelle solution was processed for TEM analysis after 24 hours of incubation (**Fig. S9**). These thiolated PEG_{10K}-*b*-PPA_{4K}/DNA micelles prepared at different DMF concentrations exhibited similar particle size and shapes as their crosslinked counterparts shown in Fig. 4.

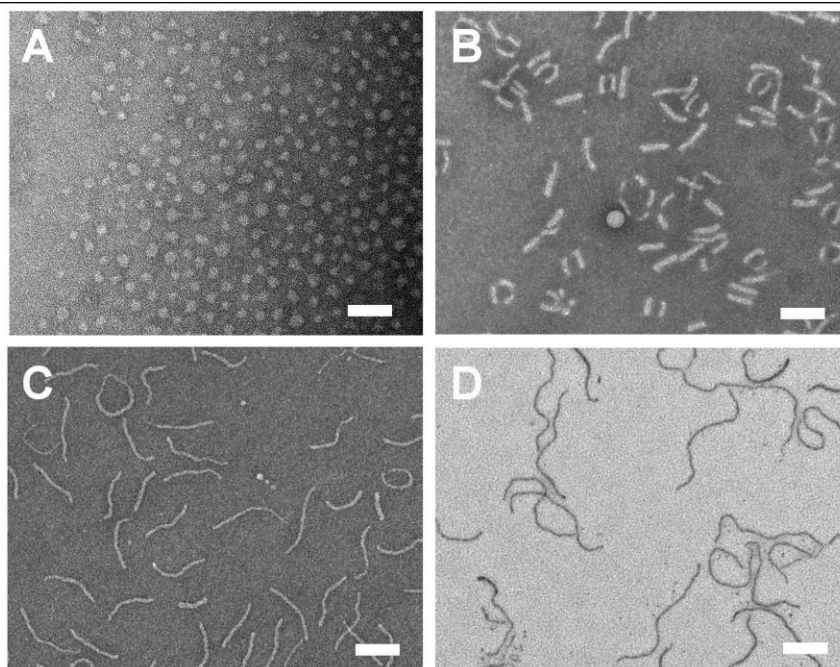


Figure S9. Morphologies of thiolated PEG_{10K}-*b*-PPA_{4K}/DNA micelles before crosslinking. Micelles with different shapes were prepared using thiolated PEG_{10K}-*b*-PPA_{4K} in 7:3 (v/v) (A), 5:5 (v/v) (B), 4:6 (v/v) (C), and 1:9 (v/v) (D) DMF–water mixtures under the same conditions as described in Fig. 4. All scale bars represent 200 nm.

4.3. Crosslinking of thiolated PEG_{10K}-*b*-PPA_{4K}/DNA micelles with different shapes

The thiolated PEG_{10K}-*b*-PPA_{4K} was then used for the preparation of micelles in the presence of 7:3 (v/v) DMF–water mixture. To transform the morphology of thiolated PEG_{10K}-*b*-PPA_{4K}/DNA micelles, DI water was titrated into micelle solution as described in Section 3. After transformation, the micelles were incubated at room temperature for 24 h and then subjected to aerial oxidation for 48 h under stirring (**Fig. S10**). DMF was then removed by

dialyzing the micelle solution against DI water using dialysis tubing with MWCO of 3,500 for another 24 h. The TEM images of crosslinked PEG_{10K}-*b*-PPA_{4K}/DNA micelles with different morphologies (Fig. 4A–D) were analyzed with Image J 1.43.

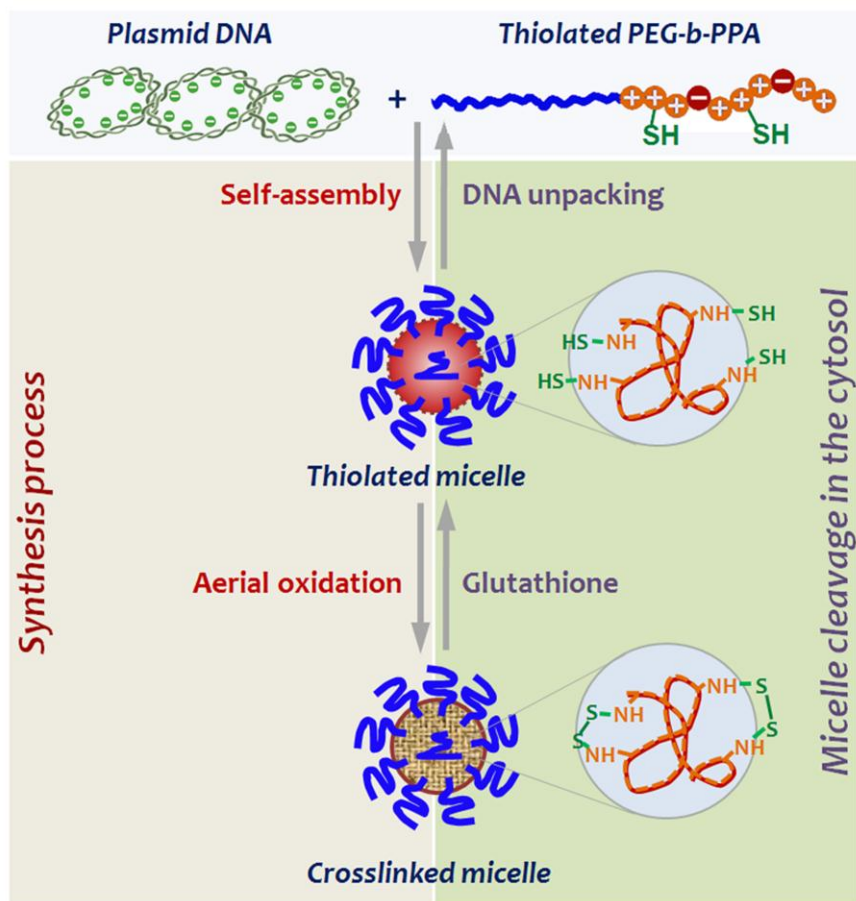


Figure S10. Preparation steps of crosslinked PEG_{10K}-*b*-PPA_{4K}/DNA micelles by aerial oxidation (left). The disulfide crosslinks can be reduced in the presence of high concentrations of glutathione found in the cytosol or nucleus. This process can then facilitate the release of DNA from the micelles (right).

4.4. Stability of crosslinked PEG_{10K}-*b*-PPA_{4K}/DNA micelles

To evaluate the stability of micelles in the presence of salts at physiological concentration, a calculated amount of NaCl solution (5 M) was added to micelles with various shapes prepared and crosslinked under the same condition as described in Fig. 4, to adjust the concentration of NaCl to 0.15 M. After incubation with NaCl for 30 minutes, an aliquot of micelle solution was processed for TEM analysis (**Fig. S11**). No micelles showed a significant change in particle size or morphology, indicating that they were insensitive to electrostatic screening.

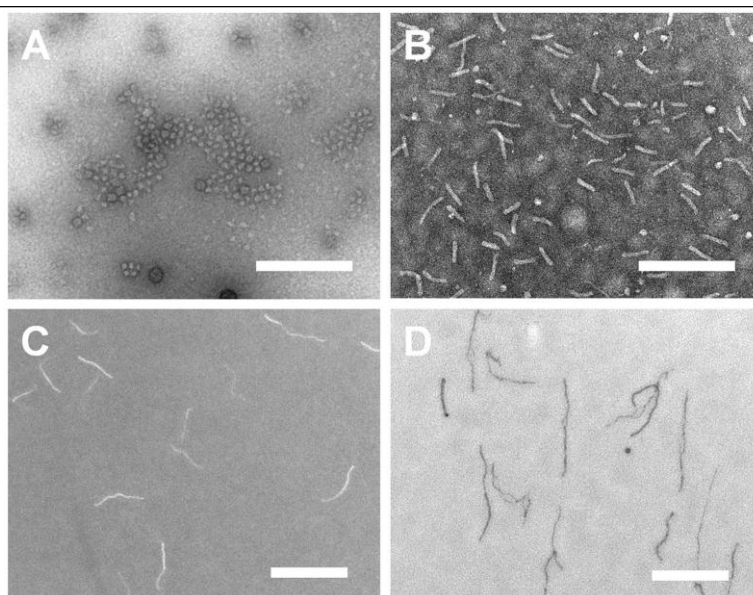


Figure S11. TEM images of crosslinked PEG_{10K}-*b*-PPA_{4K}/DNA micelles initially prepared in 7:3 (v/v) (A), 5:5 (v/v) (B), 4:6 (v/v) (C), and 1:9 (v/v) (D) DMF–water mixtures, followed by incubation in 0.15 M NaCl for 30 min. All scale bars represent 500 nm.

To assess the stability of crosslinked micelles in the presence of serum, we selected crosslinked, spherical, and worm-like micelles and incubated them in 5% (v/v) fetal bovine serum at 37°C for 1 h. An aliquot of micelle solution was then analyzed by TEM using the same method as described above. As shown in **Fig. S12A–D**, both spherical and worm-like micelles retained their original size and morphology upon incubation in serum-containing medium. In contrast, PPA_{4K}/DNA nanoparticles aggregated severely under the same condition (**Fig. S12F**).

These results demonstrate that the crosslinked micelles exhibit much higher colloidal stability and are capable of maintaining micelle size and morphology in serum-containing medium.

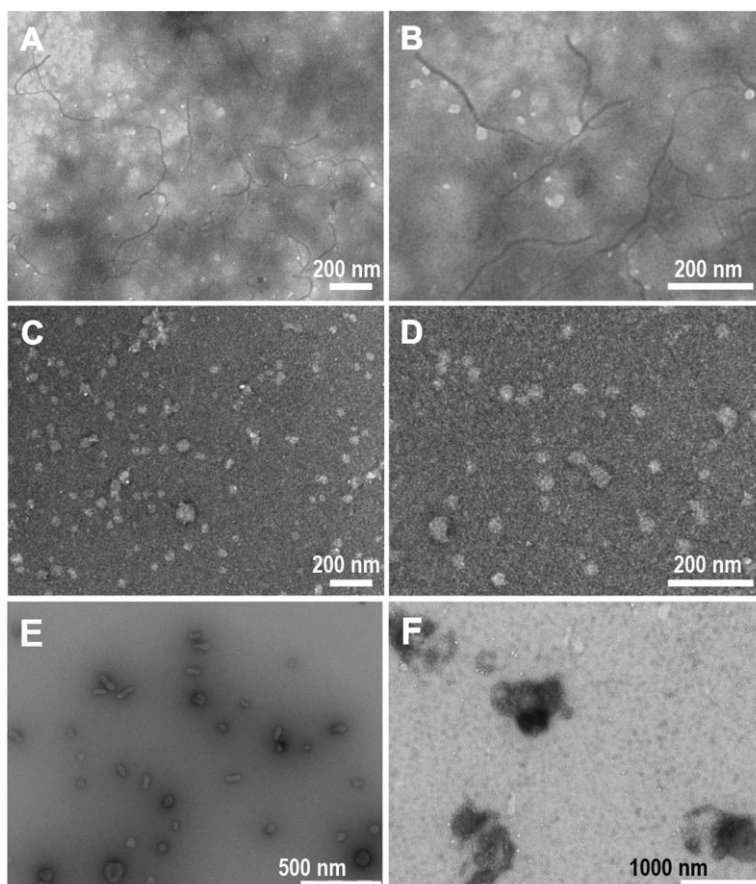


Figure S12. TEM images of crosslinked PEG_{10K}-*b*-PPA_{4k}/DNA micelles initially prepared in 1:9 (v/v) (A and B) and 7:3 (v/v) (C and D) DMF–water mixtures, followed by incubation in 5% (v/v) fetal bovine serum for 60 min at 37°C. Images for the same set of micelles prior to incubation in serum-containing medium are shown in Fig. S11D and S11A, respectively. Also shown are PPA_{4k}/DNA nanoparticles before (E) and after (F) incubation in 5% (v/v) serum under the same conditions. Image (F) reveals severe aggregation.

Furthermore, to determine whether crosslinked micelles can protect encapsulated DNA from enzymatic degradation in serum, we incubated crosslinked micelles in 10% (v/v) fetal bovine serum at 37°C for 4 h. Subsequently, DTT and heparin were added to micelle solutions to resolve the disulfide crosslinks and release the encapsulated DNA for assessment of its integrity.

An aliquot of micelle solution was analyzed by electrophoresis on a 0.8 w/v% agarose gel for 45 min at 75 V. The results are shown in **Fig. S13**. On the gel, degradation of plasmid DNA was observed after incubation for only 15 min, as indicated by a long smear band; a 2-h incubation with 10% (v/v) serum yielded nearly completely degraded plasmid DNA (Lane 10). In contrast, DNA recovered from crosslinked spherical (Lane 2) and worm-like micelles (Lane 4), which were incubated in 10% (v/v) serum at 37°C for 4 h, showed migration patterns similar to DNA samples recovered from micelles that were not incubated with serum (Lanes 3 and 5, respectively). By comparing Lanes 3, 5, and 6, it is obvious that the DNA recovering process was not fully efficient and that there was some difference in DNA release ability between spherical and worm-like micelles. But it is also clear that crosslinked micelles protected encapsulated DNA from degradation, as DNA samples recovered from micelles incubated in

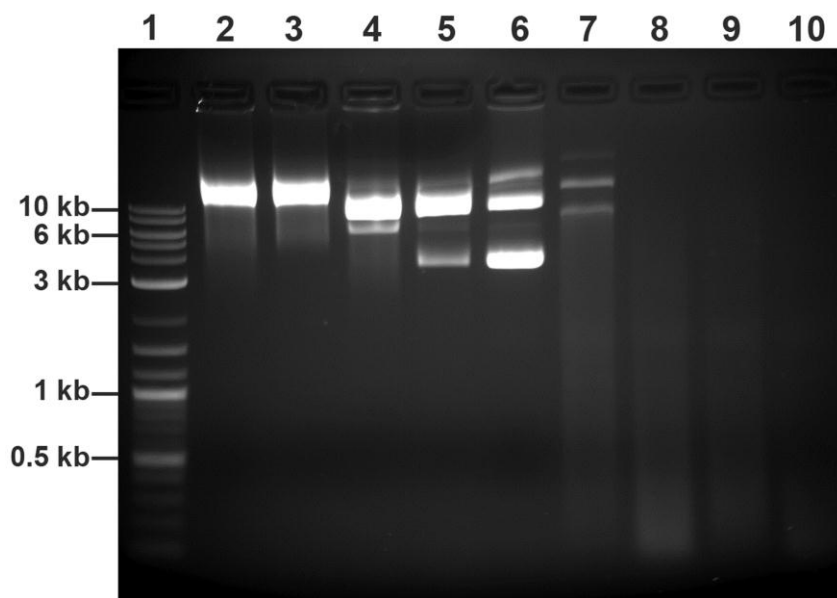


Figure S13. Stability of crosslinked PEG_{10K}-*b*-PPA_{4K}/DNA micelles with different morphologies in the presence of serum characterized with gel electrophoresis. **Lane 1:** DNA ladder, **Lanes 2 and 4:** spherical and worm-like micelles (crosslinked PEG_{10K}-*b*-PPA_{4K}/DNA micelles obtained in 7:3 (v/v) and 1:9 (v/v) DMF–water mixtures, respectively) incubated in 10 v/v% fetal bovine serum (FBS) at 37°C for 4 h, and then treated with 1 M DTT, 8 mg/mL heparin, and 20 mM EDTA at 37°C for 3 h to release encapsulated DNA. **Lanes 3 and 5:** spherical and worm-like micelles without incubation in serum-containing medium were treated similarly with DTT, heparin and EDTA to release encapsulated DNA. **Lanes 6–10:** VR1255 plasmid DNA incubated in 10 v/v% FBS for 0 min, 15 min, 30 min, 1 h, and 2 h, respectively. Smear bands in lanes 7–9 indicate severe degradation, whereas DNA in Lane 10 is nearly completely degraded.

serum-containing medium (Lanes 2 and 4) were free from low-molecular-weight DNA fragments like those shown in Lanes 7 through 10. These results confirm that the micelles provided a high level of protection to the encapsulated DNA against degradation in serum-containing medium.

4.5. *In vivo* transfection efficiency of crosslinked PEG_{10K}-b-PPA_{4K}/DNA micelles with different shapes via intrabiliary infusion

Animal studies were conducted under an animal protocol that was approved by the Johns Hopkins School of Medicine Institutional Animal Care and Use Committee (IACUC #RA09A447). Female Wistar rats aged 6–8 weeks (200–300 g) were anesthetized with intraperitoneal injection of Ketamine (100 mg/kg) and Xylazine (10 mg/kg). A 33-gauge needle was inserted into the common bile duct and the needle was secured by tie around the common bile duct. Four ml of crosslinked PEG_{10K}-b-PPA_{4K}/DNA micelles with different shapes containing 20 µg VR1255 DNA in 5% glucose solution were infused through the bile duct over 20 min with a syringe pump. A tie was then placed around the bile duct between the liver and the point of infusion to prevent back flow before the needle was withdrawn. Occasionally, stitches with 10-O nylon (Ethicon, Somerville, NJ) were needed to repair the needle hole in the bile duct to prevent bile leakage.

After intrabiliary infusion, the luciferase expression level in rat liver was characterized with Bioluminescence (BLI). BLI has been shown as a highly sensitive analysis technique for the determination of luciferase expression *in situ* [S14]. Moreover, Rettig *et al.* have reported an excellent linear relationship between *in situ* BLI measurement of the luciferase expression levels and chemiluminescence measurement in liver homogenates over a wide range of luciferase expression (from 10 pg to 5×10^5 pg luciferase per liver) [S15]. Combined with the ease and non-invasiveness of this analysis method, and the ability to monitor transgene expression in the same experimental animal over an extended period of time, this method has been widely adopted as an attractive alternative to the chemiluminescence assay. As a preliminary test, we compared the transgene of luciferase at 4 h after intrabiliary infusion. Rats were anesthetized and 1 ml of D-luciferin solution (30 mg/mL) was injected intraperitoneally. The rats were then transferred

from the box to the nose cones attached to the manifold in the imaging chamber of an IVIS Spectrum Imaging System. The rats were positioned with abdomen side up. After 5 min, the bioluminescence signals of the rats were imaged and recorded for 1 min on the IVIS Spectrum Imaging System. For rats with extremely high level of luciferase expression, saturation of BLI signal was observed; and the imaging time was reduced to 15 sec to make sure the kinetics of BLI reaction was in the linear range [S15]. The level of luciferase expression was then normalized and reported as the total photon counts in the region of interest (ROI) per second as shown in **Fig. 4h**.

4.6. Transfection efficiency and cell uptake efficiency of shaped micelles in HEK293 cells

As an initial test, we characterized the *in vitro* transfection efficiency of micelles with various shapes using human embryonic kidney (HEK) 293 cells. HEK293 cells were maintained in Dulbecco's Modified Eagle's Medium supplemented with 10% fetal bovine serum (complete medium) at 37°C and 5% CO₂. At 24 h prior to the transfection experiment, cells were seeded in 48-well plates at a density of 5×10^4 cells/well. Immediately before transfection, the culture medium was replaced with fresh complete medium. Crosslinked PEG-*b*-PPA/DNA micelles were added to each well at an equivalent dose of 1 µg of plasmid DNA per well. The culture medium was refreshed again 4 h later. After 48 h, the culture medium was removed. Cells were washed with 0.5 ml of pH 7.4 PBS, lysed with reporter lysis buffer (Promega, Madison, WI), and subjected to two freeze-thaw cycles. The lysate was centrifuged at 14,000 rpm for 5 min. The luciferase activity in the supernatant was assayed with luciferase substrate (Promega) on a luminometer (20/20n, Turner BioSystems, Sunnyvale, CA). The luciferase activity was converted to the amount of luciferase expressed using recombinant luciferase (Promega) as the standard and normalized against total protein content in the cell lysate using the BCA protein assay (Pierce, Rockford, IL).

The transfection efficiencies of these micelles are shown in **Fig. S14A**. The spherical and rod-like micelles exhibited significantly higher levels of gene transfection efficiency than the worm-like micelles. The rod-like micelles showed 2- and 16-fold higher transfection efficiency than worm-like micelles with an average length of 331 nm and 581 nm, respectively.

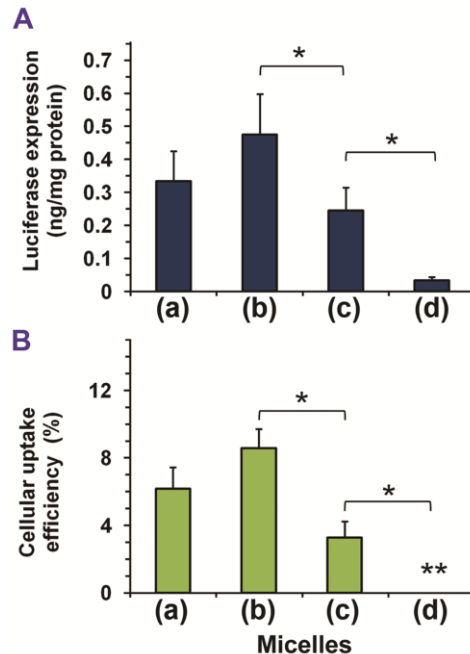


Figure S14. Transfection efficiencies (A) and cell uptake efficiencies (B) of crosslinked micelles with different shapes in HEK293 cells. Micelles with different shapes were prepared using a thiolated PEG_{10K}-*b*-PPA_{4K}, crosslinked and purified according to the same conditions as described in Fig. 4. Micelles (a)–(d) correspond to Fig. 4(a)–(d). Bars represent the average \pm standard deviation ($n = 4$). * denotes statistically significant comparison ($p < 0.05$) by the Student's *t* test.

To characterize cell uptake of crosslinked micelles, we first radiolabeled plasmid DNA with tritium. VR1255 plasmid DNA was methylated with CpG methyl transferase (M.SssL) (New England Biolabs, Ipswich, MA) and S-adenosyl-L-[(methyl)-³H] methionine (PerkinElmer, Waltham, MA) according to the protocol recommended by the manufacturer. In summary, nuclease-free water, 10 \times NEB buffer, S-adenosyl-L-[(methyl)-³H] methionine, plasmid DNA, and M.SssL were mixed sequentially. The mixture was then incubated at 37 $^{\circ}$ C for 2 h. The reaction was quenched by heating at 65 $^{\circ}$ C for 20 min. The radiolabeled DNA was purified using Miniprep plasmid extraction Kit (Qiagen, Valencia, CA). The specific radioactivity of labeled DNA was determined by spiking a known amount of DNA solution in 20 ml of scintillation fluid (Ultima GoldTM, Perkin Elmer). The radioactivity was quantified as disintegrations per minute (DPM) using a liquid scintillation counter (TRI-CARB 1900 TR, Packard, Downers Grove, IL) and expressed as DPM/ μ g of DNA.

The radiolabeled DNA was mixed with non-radiolabeled DNA at a weight ratio of 1:10. The radioactivity of the mixed plasmid was denoted as R_{total} (DPM/per μg of DNA). We then prepared crosslinked PEG-*b*-PPA/DNA micelles with different shapes using ^3H -labeled plasmid DNA according to the method described in Section 4.2. At 24 h prior to transfection, HEK293 cells were plated in a 48-well plate at a density of 5×10^4 cells per well. The transfection was conducted according to the same procedure described above using the ^3H -labeled micelles in triplicates. At 4 h after transfection, the medium in each well was carefully removed, and the cells were washed with 500 μl of PBS. The medium and washing buffer from each well were combined. The radioactivity in this combined solution (denoted as $R_{\text{supernatant}}$) was measured on a liquid scintillation counter (TRI-CARB 1900 TR, Packard, Downers Grove, IL). The cell uptake of micelles was calculated according to

$$\text{Cell uptake of } ^3\text{H}\text{-labeled DNA (\%)} = (1 - R_{\text{supernatant}} / R_{\text{total}}) \times 100\%$$

The cell transfection efficiencies (**Fig. S14A**) closely tracked their cellular uptake efficiencies measured using micelles prepared with tritium-labeled DNA (**Fig. 14B**), suggesting that poor cellular uptake of worm-like micelles is the limiting step in their transfection efficiency. The electroneutrality of the micelle surface, although potentially responsible for the lower cell uptake of all four types of micelles ($\leq 8.6 \pm 1.2\%$) compared to PPA/DNA nanoparticles ($29.9 \pm 3.6\%$), is highly beneficial to nanoparticle stability in physiological media. We anticipate that the cell uptake may be improved by incorporating cell-specific ligands on the micelle surface, which will then further enhance their transfection activities.

Supporting References:

- S1. M.C. O'Sullivan, D.M. Dalrymple, A one-step procedure for the selective trifluoroacetylation of primary amino-groups of polyamines. *Tetrahedron Lett.* **1995**, *36*, 3451.
- S2. Y. Ren, X. Jiang, D. Pan, H.Q. Mao, Charge density and molecular weight of polyphosphoramidate gene carrier are key parameters influencing its DNA compaction ability and transfection efficiency. *Biomacromolecules* **2010**, *11*, 3432.
- S3. X. Jiang, D. Leong, Y. Ren, Z. Li, M.S. Torbenson, H.Q. Mao, String-like micellar nanoparticles formed by complexation of PEG-b-PPA and plasmid DNA and their transfection efficiency. *Pharm Res.* **2011**, *28*, 1317.
- S4. S. Plimpton. Fast parallel algorithms for short-range molecular-dynamics. *J. Comput. Phys.* **1995**, *117*, 1.
- S5. Q. Liao, A.V. Dobrynin, M. Rubinstein, Molecular dynamics simulations of polyelectrolyte solutions: Nonuniform stretching of chains and scaling behavior. *Macromolecules*, **2003**, *36*, 3386.
- S6. M.J. Stevens, K. Kremer, The nature of flexible linear polyelectrolytes in salt-free solution - a molecular-dynamics study. *J. Chem. Phys.*, **1995**, *103*, 1669.
- S7. A. C. Kumbharkhane, S. M. Puranik, S. C. Mehrotra, Dielectric-relaxation studies of aqueous N,N-dimethylformamide using a picosecond time domain technique. *J. Solution Chem.*, **1993**, *22*, 219.
- S8. R.J. Hunter (1981) *Zeta Potential in Colloid Science: Principles and Applications*, (Academic Press, London), pp. 31–32.
- S9. F.E. Bailey, J.V. Koleske, in *Poly(ethylene Oxide)*, Academic Press, New York, USA, **1976**.
- S10. H.W. Diehl, E. Eisenriegler, Universal shape ratios for open and closed random-walks: exact results for all d . *J. Phys. A-Math. Gen.*, **1989**, *22*, L87.
- S11. K. Šolc, Shape of a random-flight chain. *J. Chem. Phys.*, **1971**, *55*, 335.
- S12. D. Frenkel, B. Smit, *Understanding Molecular Simulation*, 2nd Ed, Academic Press, San Diego, USA, **2002**.

- S13. C.C.Q. Chin, F. Wold, The use of tributylphosphine and 4-(aminosulfonyl)-7-fluoro-2,1,3-benzoxadiazole in the study of protein sulfhydryls and disulfides. *Anal. Biochem.*, **1993**, *214*, 128.
- S14. K.R. Zinn, T.R. Chaudhuri, A.A. Szafran, D. O'Quinn, C. Weaver, K. Dugger, D. Lamar, R.A. Kesterson, X. Wang, S.J. Frank, Noninvasive bioluminescence imaging in small animals. *ILAR J.* **2008**, *49*, 103.
- S15. G.R. Rettig, M. McAnuff, D. Liu, J.S. Kim, K.G. Rice, Quantitative bioluminescence imaging of transgene expression *in vivo*. *Anal. Biochem.* **2006**, *355*, 90.